Coherent structures of the near field flow in a self-oscillating physical model of the vocal folds

Jürgen Neubauer[a)] and Zhaoyan Zhang
The Laryngeal Dynamics Laboratory, UCLA School of Medicine, 31-24 Rehabilitation Center, 1000 Veteran Ave., Los Angeles, California 90095

Reza Miraghaie
Department of Mechanical and Aerospace Engineering, UCLA, Los Angeles, California 90095

David A. Berry
The Laryngeal Dynamics Laboratory, UCLA School of Medicine, 31-24 Rehabilitation Center, 1000 Veteran Ave., Los Angeles, California 90095

Current theories of voice production depend critically upon knowledge of the near field flow which emanates from the glottis. While most modern theories predict complex, three-dimensional structures in the near field flow, few investigations have attempted to quantify such structures. Using methods of flow visualization and digital particle image velocimetry, this study measured the near field flow structures immediately downstream of a self-oscillating, physical model of the vocal folds, with a vocal tract attached. A spatio-temporal analysis of the structures was performed using the method of empirical orthogonal eigenfunctions. Some of the observed flow structures included vortex generation, vortex convection, and jet flapping. The utility of such data in the future development of more accurate, low-dimensional models of voice production is discussed. © *2007 Acoustical Society of America.* [DOI: 10.1121/1.2409488]

I. INTRODUCTION

Traditionally, according to the linear source-filter theory of voice production, the glottal volume velocity is considered to be the sound source of the human voice (Fant, 1960; see, e.g., Stevens (1998), for extensive review). However, this theory relies heavily on assumptions about the voice source, the vocal tract filter, and the independence of the source and filter, which have never been formally validated for normal (modal) phonation, and much less for nonmodal states of phonation such as may occur in dysphonia, or at phrase and sentence boundaries in English. In addition to neglecting possible source-tract interactions, another critical limitation of the linear source-filter theory of voice production may be its dependence on one-dimensional, scalar field theory. McGowan (1988) maintained that a full three-dimensional description of the fluid velocity field at glottal exit was required to accurately model the voice source. First, he argued that a nonacoustic (rotational, incompressible) component of the glottal velocity field, separate from the glottal volume velocity, was required to accurately predict the oral acoustic output. Second, he argued that vortex structures in the glottal near field produced a fluctuating force on the vocal folds. In particular, he contended that vortex structures were produced during glottal opening, and that the roll-up, acceleration and downstream convection of such structures resulted in an upstream force on the vocal folds. Thus, McGowan (1988) proposed a flow feedback mechanism, which directly impacted

vocal fold dynamics, and hence sound generation within the larynx. Krane (2005) proposed a similar mechanism for unvoiced speech production.

Similarly, Hirschberg *et al.* (1996) has argued that the flow separation point and the area of the glottal jet, as assumed by most advanced computational models of vocal fold vibration, are only crude, first-order approximations. They contend that the flow separation point and the area of the glottal jet cannot be accurately approximated without a full knowledge of the near field flow structures immediately downstream of the glottis. Indeed, based on major discrepancies between theory and experiment, Hofmans *et al.* (2003) concluded that "the structure of the jet flow" was critical for modeling the sound source, and predicting the oral acoustic output. Indeed, many investigators have probed the possible contributions of three-dimensional source mechanisms in voice production (Barney *et al.*, 1999; Hirschberg, 1992; Hofmans, 1998; Hofmans *et al.*, 2001a, b; Howe and McGowan, 2005; Krane, 2005; McGowan, 1988; McGowan and Howe, 2006; Shadle *et al.*, 1999; Zhang *et al.*, 2002).

Despite such investigations, only a few attempts have been made to quantify the near field flow structures immediately downstream of the glottis. The primary measurement technique which has been used to quantify particle velocities in this region has been single-fiber, hot-wire anemometry, a method which assumes that particle velocities are nonzero only in the inferior-superior direction, and that in this direction, the velocities are non-negative. However, if complex three-dimensional fluid structures were to exist within the
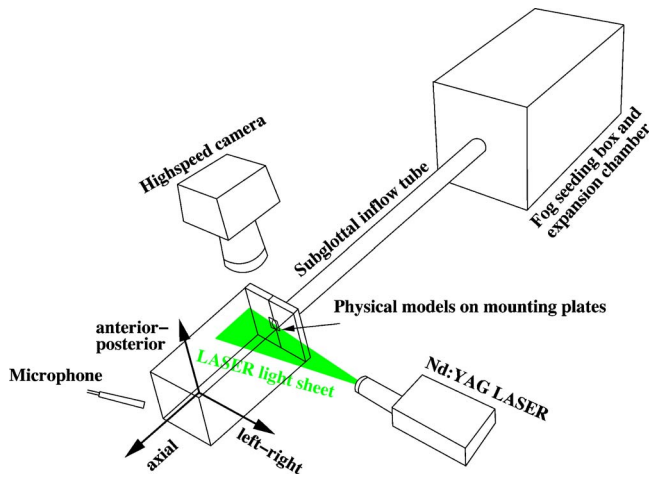

FIG. 1. (Color online) Experimental setup for flow visualization of glottal jet: Expansion chamber with the theatrical fog machine for flow seeding, straight cylindrical inflow tube, pair of physical vocal fold models, high speed camera, and Nd:YAG LASER with LASER sheet module. The axial direction is perpendicular to the plane of the mounting plates. Note that for the digital particle image velocimetry (DPIV) experiments we mounted a large rectangular duct downstream from the mounting plates to increase mixing and thus seeding density in the entrainment region of the glottal jet (duct dimensions: 25.4 cm × 12.7 cm × 12.7 cm).

near field flow, then hot-wire anemometry would not be an appropriate technique to quantify such structures.

In order to circumvent possible problems with the technique of hot-wire anemometry, we use the methods of flow visualization and particle image velocimetry to study the near field flow structures of a self-oscillating, physical model of the vocal folds, with a vocal tract attached. Using the method of empirical eigenfunctions, we conduct a spatio-temporal analysis of the near field flow structures. Specifically, we address the following questions: what are the most significant spatio-temporal structures of the near field flow? Are these structures similar to ones which have been reported previously for static models of the glottis? Do these structures suggest feedback mechanisms between the near field flow and the larynx? And what possible implications do such structures have on voice production?

II. MATERIALS AND METHODS

A. General experimental setup

The general setup for our experiments is shown in Fig. 1. It consisted of an expansion chamber, a straight inflow tube, a pair of physical models of the vocal folds, a LASER light sheet, and a high speed camera. The volumetric flow rate of the pressurized air supplied to the expansion chamber was measured with a precision mass flowmeter (type 558A, MKS). The expansion chamber was used to acoustically terminate the inflow tube on the upstream side with a defined acoustical impedance. It could be regarded as an experimental equivalent to the bronchi and lungs in humans. It was made of 1.27-cm-thick Plexiglas, was about 50.8 cm long, and had an inner cross section of 23.5 cm × 25.4 cm (volume: approx. 30.3 l). A theatrical fog machine (Chauvet Hurricane Fogger F-650) inside the expansion chamber was used to seed the air flow with tracer particles for flow visualization

and digital particle image velocimetry (DPIV) measurements. Downstream from the expansion chamber, we placed a straight cylindrical PVC tube (inner diameter 2.54 cm). We used two inflow tube lengths, a 69-cm-long tube with quarter-wavelength frequency of approx. 125 Hz and an 81-cm-long tube with a quarter-wavelength frequency of about 106 Hz. The ratio of the cross-sectional areas of the expansion chamber and the subglottal inflow tube was approx. 117. Therefore, we assumed that on the upstream side the inflow tube had an acoustic termination equivalent to an ideal open end. The measured reflection factor reported in Zhang *et al.* (2006) confirmed this assumption.

The physical models glued into grooves in two acrylic mounting plates were placed at the downstream end of the subglottal inflow tube. Details on the fabrication and dynamic characteristics of the physical model were reported elsewhere (Thomson, 2004; Thomson *et al.*, 2005, 2004). In brief, they were made from a two-component liquid polymer solution mixed with a liquid flexibilizer solution. The models were approx. 1.2 cm high (superior-inferior dimension) and 0.8 cm wide (medial-lateral direction). The model lengths (in anterior-posterior direction) were 1.7 and 2.3 cm, respectively. The physical properties of both sets of models were identical and as reported in Thomson *et al.* (2005). Note that the oscillation frequencies of both sets were similar to the quarter-wavelength resonance frequency of the used subglottal inflow tube. For a detailed report on the influence of the acoustics of the subglottal inflow system see Zhang *et al.* (2006).

The sound pressure downstream from the physical model was measured with a 1.27-cm-diam microphone (4193-L-004, B&K, Denmark). The microphone was connected to a conditioning amplifier (NEXUS 2690, B&K, Denmark) where the signal was bandpass filtered between 20 Hz and 22.4 kHz. The filtered signal was monitored with a digital storage oscilloscope and recorded with a standard PC sound card at a sampling rate of 100 kHz and 24 bit resolution for a voltage range of ±1.0 V. The microphone was calibrated with a B&K sound level calibrator (type 4231).

During the flow visualization and DPIV experiments with a double-pulsed LASER, the LASER pulses were not locked to specific phases of the model oscillation. Instead, we simultaneously recorded the far field sound pressure and a trigger signal generated from the LASER unit before each double pulse. As shown in Fig. 2, the far field sound pressure spectrum was harmonic. Thus, *a posteriori* we could select series of "snapshots" where the oscillating flow was repeatedly illuminated at approx. similar phases. The selected snapshots were "quasi-phase-locked" representations of the time-dependent periodic flow field. As the fundamental frequency f_0 depended weakly on the subglottal flow rate, we recorded a different number N_T of phases per period T due to the repetition rate f_{rep} of the double-pulsed LASER. The fundamental frequency f_0 was $f_0 = f_{rep}(n + 1/N_T)$ where the integer n is the number of oscillation cycles between consecutive double pulses of the LASER (f_{rep} is the repetition rate of the double pulses.).
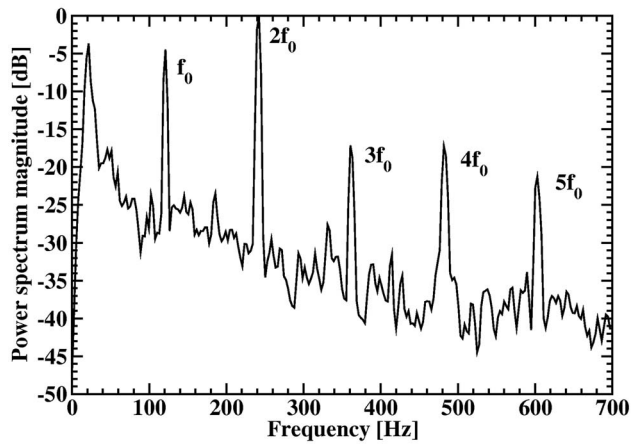
FIG. 2. Normalized power spectrum of the sound pressure signal during the flow visualization measurements. Note that the second harmonic $(2f_0)$ is significantly stronger than the fundamental frequency (f_0). The peak at about 20 Hz is an artifact due to high-pass filtering of the microphone signal. $(f_0 \approx 122$ Hz, volumetric flow rate approx. 480 ml/s, subglottal inflow tube: 69 cm, physical model length: 1.7 cm).
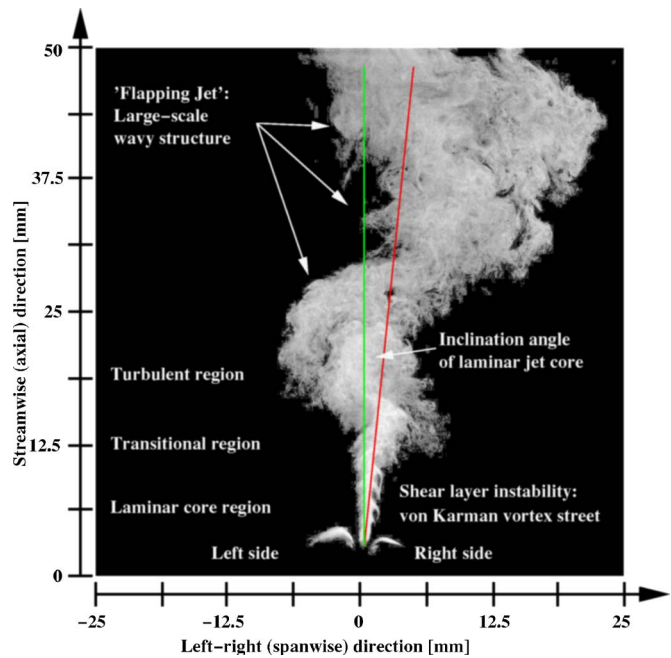

FIG. 3. (Color online) Representative flow visualization image during model oscillation: The superior edges of the left and right model sides were illuminated by the LASER light sheet. The direction of the streamwise jet axis is indicated by the red line. (volumetric flow rate about 480 ml/s, subglottal inflow tube length: 69 cm, physical model length: 1.7 cm).

B. Quasi phase-locked flow visualization with LASER light sheet

A qualitative analysis of coherent flow structures of the glottal jet was done using the images from the quasi phase-locked flow visualization experiments. Typical for flow visualization, the seeding density was high in the seeded flow regions and low outside. In flow regions where the mixing was small, the scattered LASER light from the seeded flow showed mainly the dynamics of the boundaries between seeded and unseeded flow. In flow regions with large mixing, boundaries between seeded and unseeded flow disappeared and only the motion of large-scale patches of seeded flow ("blobs") could be identified by eye as "coherent structures" (see Fig. 3).

For flow visualization with a LASER light sheet, the beam from a double-pulsed Nd:YAG LASER (Solo III PIV 15, New Wave Research, Fremont, CA) was shaped into a thin light sheet (approx. 1 mm thick) with a light sheet module (Dantec Dynamics, Denmark) mounted to the LASER head. Each pulse from the double-pulse LASER had about 5 mJ light energy and a pulse duration of about 3–5 ns. The interpulse interval of the double pulses of the LASER was $\Delta t = 0.25$ ms or $\Delta t = 0.5$ ms, respectively. The repetition rate of the double-head LASER was 15 Hz. The scattered light from the tracer particles in the seeded glottal jet was observed with a high speed camera (Fastcam-Ultima APX, Photron USA, San Diego) and a 58 mm lens (Noct NIKKOR, Nikon, USA) with one 14 mm extension ring. The CMOS array of the camera contained 1024×1024 pixels to capture the scattered light from the selected field of view downstream from the physical model. The recording frame rate of the high speed camera was 2000 frames/s (for interpulse interval $\Delta t = 0.5$ ms) and 4000 frames/s (for $\Delta t = 0.25$ ms), respectively. Two light sheet orientations with respect to the physical model and the glottal jet were used for the illumination of the seeded jet flow: First, the light sheet was placed in an axial and left-right direction to observe the

medial-lateral dynamics of the glottal jet at the midline of the physical model (shown in Figs. 3, 5, 7, and 9). Second, the glottal jet flow in anterior-posterior direction was observed with a light sheet oriented in an axial and anterior-posterior direction to assess the three-dimensional structure of the glottal near field flow (shown in Fig. 10).

Figure 3 shows one representative flow visualization image where some general flow features can be seen. Note that at the bottom of Fig. 3, the superior edges of the left and the right sides of the physical model can be seen being illuminated by the LASER light sheet. The glottal jet within some small part of the glottal exit channel was also visible.

C. Digital particle image velocimetry (DPIV)

We used DPIV measurements to quantitatively observe coherent flow structures in the glottal near field flow. In contrast to flow visualization, the flow velocity field in the entrainment region outside the laminar core region could also be observed. The field of view of the DPIV measurements was restricted to about half the size of the flow visualization images. Therefore, we focused on the dynamics of the laminar core region with the roll-up of large-scale vortices and the convection of these vortices into the turbulent region (see Fig. 4). Thus, DPIV is an extension of flow visualization in both the resolved region of air flow and the flow field information in terms of flow velocities instead of only seeding density or seeding boundaries.

For planar DPIV, we used a double-pulse Nd:YAG LASER (Solo 120, New Wave Research, Fremont, CA) with a light sheet module (LaVision, MI) to illuminate a thin slice (about 1 mm thick) of the seeded jet flow. The light sheet was oriented in the axial and left-right direction. The energy
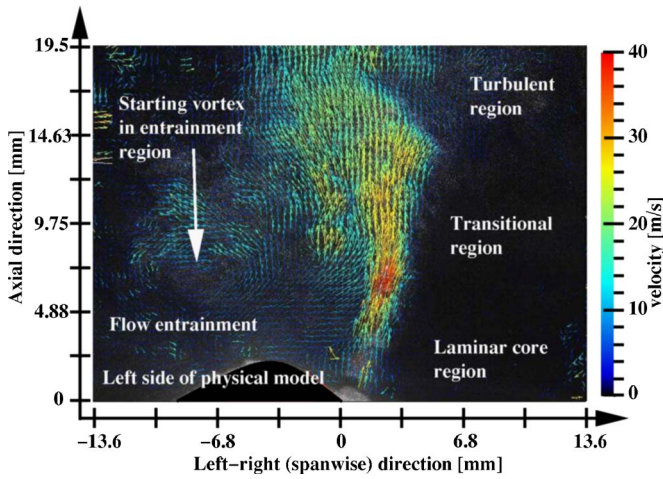
FIG. 4. (Color online) Representative velocity field from DPIV measurement of (slightly confined) glottal jet: The left side of the physical model was illuminated by the LASER light sheet. A vortex-like structure of the starting jet is visible on the left side in the entrainment region. The flow field on the right side of the model could not be resolved due to the low scattered light intensity in the shadow of the jet flow. The left and right walls of the confining downstream duct were located at approx. −63 and 63 mm in left-right direction, respectively. (volumetric flow rate approx. 480 ml/s, fundamental frequency $f_0 \approx 99.99$ Hz, subglottal inflow tube length: 81 cm, physical model length: 2.3 cm).

of each LASER pulse was about 5–10 mJ. The interpulse interval of the double pulses was $\Delta t = 5$ μs. A double-shutter camera (Image Intense, LaVision Inc., MI) with an interframe interval of 5 μs and a repetition rate of 4.95 double frames/s together with a 60 mm lens (NIKKOR, Nikon USA) was used to capture the scattered light from the tracer particles in the LASER light sheet. The CCD array of the camera contained 1376×1040 pixels that were used to capture a field of view of 27.2 mm × 19.5 mm.

For increased seeding particle density in the downstream region outside the core of the glottal jet (i.e., in the entrainment region), a rectangular acrylic duct was mounted downstream from the physical model. This also helped to isolate the jet flow from air disturbances from the laboratory environment. The duct was 25.4 cm long (in axial direction) and had a inner cross section of 12.7 cm × 12.7 cm. Therefore, the ratio of the duct width and the maximum glottal opening width ($W_{max} \approx 1$ mm) was approx. 127. This expansion ratio was large, so that influences of the confining duct wall on the glottal jet dynamics could be neglected.

Flow velocity vector fields were calculated from image pairs that were obtained from LASER double pulses. For a detailed description of the theory of DPIV we refer to, e.g., Adrian (1991); Westerweel (1997). In our experiments, the processing was done with the software package DaVis (LaVision, Inc. MI) using a multi-pass algorithm. Two passes with an interrogation window size of 64×64 pixels were followed by two passes at 32×32 pixels. The overlap of the interrogation windows was 50%.

Figure 4 shows one representative velocity field obtained from two-dimensional DPIV measurements of the glottal jet through the physical model. Only the left side of the physical model was visible in these DPIV images. The confining duct walls in Fig. 4 were located at approx. −63

and 63 mm in left-right direction. The maximum jet core velocity was approx. 40 m/s. Note that the flow vector field immediately downstream from the right model could not be resolved, because there the intensity of the scattered LASER light was too low due to low seeding density and low LASER light intensity.

D. Extraction of coherent flow structures

Coherent structures are spatially and temporally organized flow structures that are found even in turbulent flow. They are the building blocks for large-scale motions in fully developed turbulence (Holmes *et al.*, 1997; Theodorsen, 1952; Townsend, 1976). Qualitatively, coherent flow structures could be identified using the "eyeball norm" to identify small- and large-scale structures in the scattered light from the seeding concentration fields in flow visualization experiments (Sirovich *et al.*, 1990): Using a high speed camera and a double-pulsed LASER light sheet with exposure times of about 3–5 ns, we effectively "froze" the motion of the glottal jet at two time instances. If the time delay between two consecutive LASER pulses is short enough compared to the flow velocities in the observed flow field, then the trajectories of seeding structures (such as blobs and "hook-like and wave-like boundaries") can be tracked by visual inspection. This is useful especially for the characterization of small-scale, high-frequency shear layer vortices.

The technique of "principal component analysis" (PCA) can be used as an objective method to numerically extract coherent flow structures from seeding concentration fields in flow visualization experiments and from flow vector fields in DPIV experiments (Berkooz *et al.*, 1993; Holmes *et al.*, 1996; Lumley, 1967; Sirovich *et al.*, 1990). PCA provides a rational framework to decompose organized flow structures. PCA is a statistical procedure that identifies coherent, i.e., correlated dynamics in spatio-temporal patterns. As the recorded images from the flow visualization experiments and the DPIV measurements captured a superior part of the physical model, we could relate the dynamics of the coherent flow structures (here defined as the PCA eigenfunctions) to the vibrational behavior of the physical vocal fold model.

Coherent flow structures of a spatio-temporal flow field ("movie") were defined as the empirical orthonormal functions $\psi_l(\mathbf{x})$ (EOFs) obtained from PCA. The scalar-valued or vector-valued movie $f(\mathbf{x},t)$ ($\mathbf{x} \in \mathbf{R}^2$, $t \in \mathbf{R}$) is written as

$$f(\mathbf{x},t) = \sum_{\ell=1}^{N} \sigma_\ell \varphi_\ell(t) \psi_\ell(\mathbf{x}). \qquad (1)$$

The functions $\psi_l(\mathbf{x})$ capture the coherent spatial structures of the flow field movie, the functions $\varphi_l(t)$ are the corresponding temporal coefficients ("amplitudes") of the coherent structure, and σ_l were the weights of the coherent structures with respect to the total dynamics of the spatio-temporal flow field. We use the terms "topos" to refer to the spatial functions $\psi_l(\mathbf{x})$, "chronos" to refer to the temporal functions $\varphi_l(t)$, and "energy" to refer to σ_l^2 (Aubry *et al.*, 1991). For a detailed description of coherent structures based on PCA, we refer to the Appendix.

J. Acoust. Soc. Am., Vol. 121, No. 2, February 2007

Neubauer *et al.*: Coherent structures of the glottal nearfield   1105

III. RESULTS

At a subcritical flow rate of approx. 300 ml/s, in which the physical model was stationary ("prephonatory standstill"), the open model glottis discharged a steady open jet. Light sheet illumination of a left-right and axial plane in the center of the jet showed that the jet axis was inclined by approx. 8° away from the normal direction of the mounting plates towards the right model side. This side protruded less far downstream than the left model side. These observations hinted that the direction of the glottal duct during prephonatory standstill was oblique as the left and right physical models were deformed asymmetrically by the applied subglottal flow. Scherer *et al.* (2001) and Shinwari *et al.* (2003) found inclined jet axis directions for both symmetric and oblique rigid vocal fold models. They also showed that the pressure distribution in the glottal channel was asymmetric. In our experiments with deformable physical models, the model geometry during prephonatory standstill was the result of a static equilibrium of pressure forces on the physical model walls and the elastic forces of the models. Even if the elastic properties of the left and right physical model were identical, it is possible that the asymmetry in the pressure distribution on the left and right model walls would lead to an asymmetric oblique direction of the glottal channel during standstill.

For a supercritical flow rate above approx. 480 ml/s, the typical far field sound pressure of the model oscillations is as shown in Fig. 2. With this kind of physical model, we typically observed a significantly larger sound pressure amplitude at the second harmonic ($2f_0$) than for the fundamental frequency (f_0).

A. Oscillation of laminar jet core axis

Figure 5 shows an enlarged view of the seeded jet flow in the laminar core region. This cycle of double-frame images of the scattered LASER light revealed different stages of attachment and detachment of the laminar core from the physical model walls. We found this behavior to be consistent in our experiments with the physical model. At the beginning of the cycle (frame 0), when the flow rate was minimal and the model glottis was almost closed, the seeded flow stayed attached to the left side of the model (upper side in Fig. 5). This side protruded downstream further than the opposite right side, probably due to asymmetries of the mounting of the physical models onto the holding plates. During the opening phase (frames 1 and 2), when the flow rate increased, the laminar core width increased while the jet flow stayed attached to the right side of the model (lower side in Fig. 5). During maximum opening (frames 3 and 4), the jet core axis moved slightly to the center of the glottis, and the flow detached from the divergent exit wall of the right model. During the closing phase (frames 5 and 6), when the jet flow rate decreased, the laminar core width decreased and the flow reattached to the right model wall.

During maximum opening and during the closing phase (frames 3–6), the laminar core region downstream of the glottis exit was straight. During the opening phase, we observed a strongly curved flow downstream of the glottis exit: Just before opening of the model glottis (frames 0 and 7), the
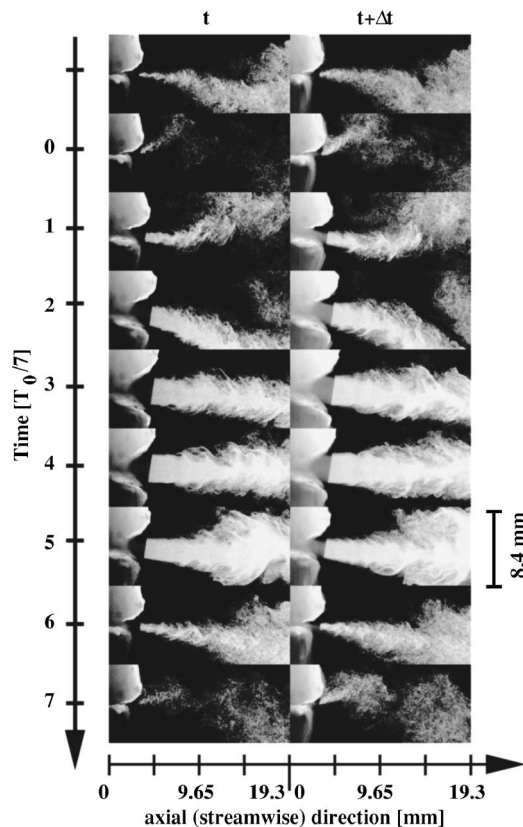

FIG. 5. Magnified view of image pairs showing the laminar core region and the transitional region for one oscillation cycle. The jet core axis oscillated in the left-right direction: During opening the flow stayed attached to the right model (lower side). It detached from the right side, while the direction of the jet core rotated to the left side. During closing, the flow reattached to the right side of the model. ($\Delta t = 0.25$ ms, $f_{rep} = 15$ Hz, volume flow rate approx. 630 ml/s, fundamental frequency $f_0 \approx 122$ Hz, subglottal inflow tube length: 81 cm, physical model length: 2.3 cm).

flow downstream from the almost closed glottis was bent towards the left model side. This might be due to the leftover recirculation from the flow in the previous cycle. This curved flow structure was convected downstream (frame 1) and the curvature changed towards the right side in a later opening phase (frame 2). The changing curvature is probably due to the influence of the jet flow in the beginning of the cycle which may produce circulation opposite to the one in frames 0 and 7.

For one oscillation cycle, we estimated the instantaneous width of the laminar core region and the instantaneous inclination angle of the laminar core axis with respect to the axial direction (the normal direction to the mounting plates) (Fig. 6). These values were measured visually from images of the seeded jet flow within and just downstream of the exit of the model glottis (as seen in Fig. 5). Positive inclination angles indicated inclination to the right model side. Figure 6 shows that the laminar jet width oscillated quasi-sinusoidally at the fundamental frequency ($T_0 = 1/f_0$). The observed core width varied between about 0.4 and 1.5 mm. The inclination angle varied about a mean value of approx. 8° with an amplitude of approx. 4°. Over one oscillation cycle, it showed a double-peak behavior: starting from about 4° at the beginning of the cycle ($t = 0$), the inclination angle increased to about 12° at about one quarter of the cycle ($t = T_0/4$)). Then the angle
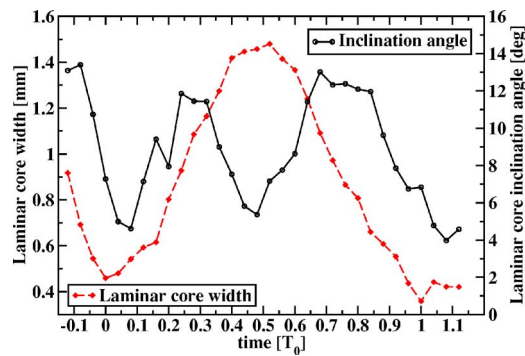
FIG. 6. (Color online) Inclination angle and width of the laminar core downstream from the physical model. The inclination angle was defined as the angle between the axial direction (perpendicular to the mounting plate of the physical model, see Fig. 1) and the instantaneous laminar core direction. Positive angles indicated a rotation towards the right side. While the width of the laminar core varied quasi-sinusoidally with the fundamental frequency, the inclination angle showed a double-peak behavior. During opening and closing (flow acceleration and deceleration), the jet axis stayed at the right side of the physical model. ($f_0 = 1/T_0 = f_{rep}(n+1/N_T) = 120.6$ Hz, where $N_T = 25$, $n = 8$, $f_{rep} = 15$ Hz, volumetric flow rate approx. 480 ml/s, subglottal inflow tube length: 69 cm, physical model length: 1.7 cm).

decreased to about $5°$ at $t = T_0/2$. In the second half of the cycle, the inclination angle increased again to about $12°$ at about $t = 3T_0/4$ and finally returned to about $4°$ at the end of the cycle. Note that the double-peak behavior was also present in the far field sound pressure as indicated by the dominant second harmonic in Fig. 2.

B. Shear layer structure

Downstream from the physical model exit, the laminar core was surrounded by a von Kármán-like vortex street indicated by the hook-like structure of the boundary of the seeded flow (Figs. 3 and 7). The width of this vortex street increased with increasing distance from the physical model, until the left and right shear layers merged and the visible hook-like structure disappeared. This widening of the shear layer was due to the convection and growth of the shear layer vortices. The flow within the glottal channel was laminar for the flow rates used in our experiments (here up to about 630 ml/s).

C. Flapping of turbulent region

Figure 7 shows the seeded jet flow in both the laminar and the turbulent region during one oscillation cycle. The disparity of image pairs recorded with a delay of $\Delta t = 0.5$ ms allowed us to visually track flow patterns in the plane of the LASER light sheet. As shown in Fig. 7, the jet flow in the transitional region reorganized into small-scale turbulent behavior organized in a large-scale wave-like pattern in the turbulent region. This wave-like pattern in the turbulent region has been termed a "flapping jet" (see Gordeyev and Thomas (2000); Thomas and Brehob (1986)). It stems from early interpretations that the jet "flaps like a flag" which would imply left-right oscillations of the instantaneous axial velocity profile. In static planar jets, the "flapping jet phenomenon" is now understood in terms of large-scale coherent structures in the turbulent region organized in
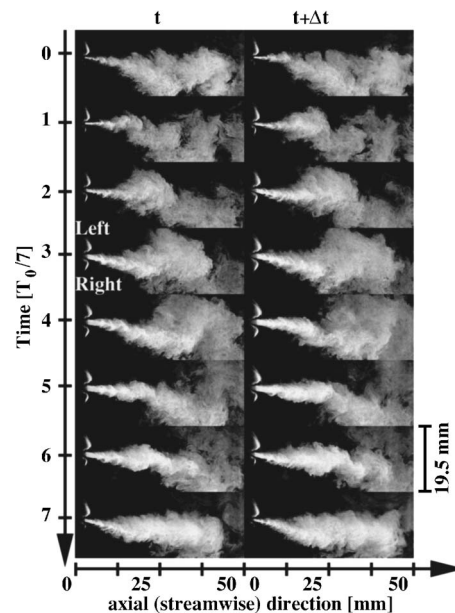

FIG. 7. Quasi phase-locked observation of the seeded open glottal jet during one oscillation cycle. A von Kármán-like vortex street in the shear layer of the laminar core and the flapping of the jet in the turbulent region can be observed. ($\Delta t = 0.5$ ms, volumetric flow rate approx. 480 ml/s, $f_{rep} = 15$ Hz, $f_0 = f_{rep}(n+1/N_T) = 121.875$ Hz, $N_T = 8$ different phases, $n = 8$, field of view: 50 mm × 50 mm, inflow tube length: 69 cm, physical model length: 1.7 cm).

an antisymmetric array of counter-rotating vortices (Gordeyev and Thomas, 2000; Thomas and Brehob, 1986). This antisymmetric vortex array convects downstream into the turbulent region while new vortex structures are created in the transitional region. Visualizing such a velocity field with seeding particles in a light sheet, the seeded flow seems to "flap" in the left-right direction.

The experiments with DPIV confirmed the observations made from flow visualization. In Fig. 8 we show a sequence of velocity vector fields for one oscillation cycle. There, the flapping of the jet in the turbulent region due to the convection of a vortex structure can be clearly seen (frames 1–3). The vortex structure downstream from the left model side was created during the opening phase. As shown above in Fig. 5, at minimal opening the flow downstream from the model was bent towards the left side. This bend then convected downstream (frame 1 in Fig. 8) and led to the observation that the jet flapped to the right side (frame 2 and 3). In frame 4, a small, wavy undulation of the jet core in the transitional and turbulent region can be seen.

The convection of large-scale plume-like structures during one cycle was visualized by spatio-temporal plots constructed by concatenating axial slices from flow visualization image pairs (Fig. 9). This spatio-temporal plot contained 49 pixel = 2.4-mm-wide slices taken from the center region of the double-pulse flow visualization images. It showed the temporal behavior of the glottal flow near field in an axial slice centered about the center of the glottal channel. Due to the convection of large-scale plumes of seeded flow and the flapping of the jet in the turbulent region, we observed inclined stripes of seeded flow in the spatio-temporal plot. The convection velocity of the large-scale structures initiated dur-
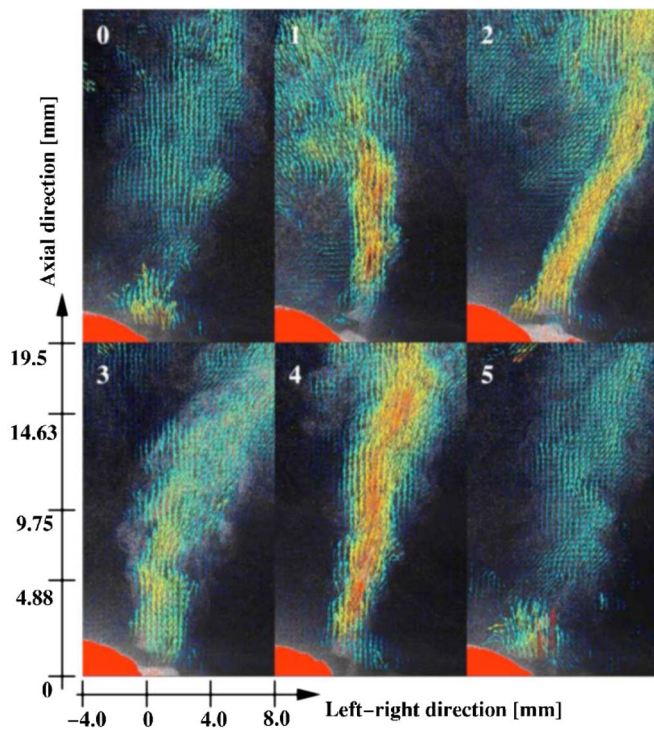
FIG. 8. (Color online) Magnified image sequence of velocity vector fields from DPIV experiments: Frame 1 corresponds to the velocity field shown in Fig. 4. In frames 0 and 5, the model glottis is minimal, but not closed. Residual flow from the previous oscillation cycle could be seen downstream from the glottal exit (frames 0 and 5). In frame 1, the glottis opened and the jet flow velocities in the laminar core increased, while the direction of the laminar core axis moved to the right side. In frames 2 and 3, the jet axis in the turbulent region flapped to the right side. In frame 3, the laminar core widened significantly while the direction of the laminar jet core axis moved back towards the left side. The largest flow velocities in the jet over the entire jet length occurred in frame 4. (volume flow rate approx. 480 ml/s, $f_0 = f_{rep}(n+1/N_T) = 99.99$ Hz where $N_T = 5$, $n = 20$, $f_{rep} = 4.95$ Hz, subglottal tube length: 81 cm, physical model length: 2.3 cm).

ing the opening phase could be estimated from the slope of the stripe-like patterns. We found convection velocities of approx. 9.7 m/s compared with jet core velocities of about 40 m/s. The convection velocity of flow structures in the middle of the oscillation cycle could be estimated as about 7.5 m/s. Note that for the location of the observation slice there were two inclined stripes for each oscillation cycle. Therefore, an observer at a fixed location in the turbulent region would observe a double-peaked seeding concentration signal for each oscillation cycle.

D. Three-dimensional flow features

Our study used only two-dimensional slices of the full three-dimensional glottal flow structure. The degree to which the glottal jet has three-dimensional features was illustrated with flow visualization experiments with the LASER light sheet in an axial and anterior-posterior plane (Fig. 10): First, we observed vortex structures in the shear layer at the anterior and posterior boundaries of the laminar core (frame 1). Second, downstream from the axially convected vortex structures, the anterior-posterior jet width decreased abruptly (frame 1). Third, at maximum opening (frame 2), we observed a converging laminar jet flow, which might be related
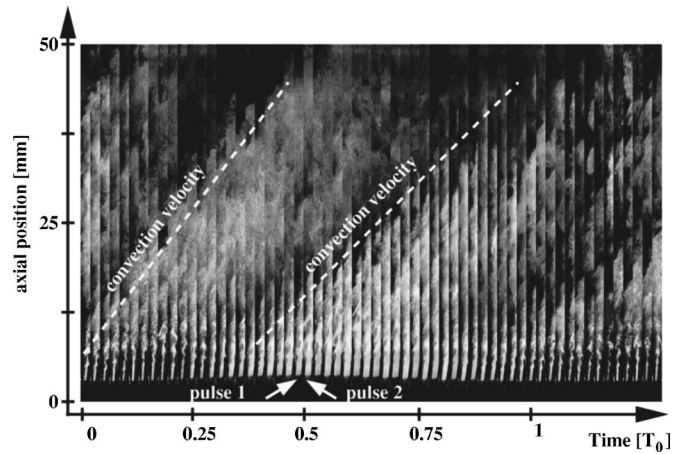

FIG. 9. Spatio-temporal plot from seeding density image pairs constructed from axial slices revealing convection of plume-like flow structures and flapping of the flow in the turbulent region: The jet flaps through the axial slices. For this cycle, the corresponding variation of the laminar core width and the inclination angle of the laminar core axis were shown above in Fig. 6. The convection velocity of the first plume-like structure could be estimated as about 9.7 m/s, the second as about 7.5 m/s. (width of concatenated slices: 49 pixel=2.4 mm, $\Delta t = 0.5$ ms, $f_{rep} = 15$ Hz, $f_0 = 1/T_0 = 120.6$ Hz with $N_T = 25$, volume flow rate approx. 480 ml/s, inflow tube length: 69 cm, physical model length: 1.7 cm).

to the axis switching phenomenon known from noncircular jets (Gutmark and Grinstein, 1999). And fourth, during closing (frame 4), the flow in the light sheet just downstream from the model broke up into two parts, one anterior and one posterior jet flow. Therefore, the flow downstream from the physical model was found to be essentially three dimensional and it showed typical features of jet flows through static noncircular orifices (Gutmark and Grinstein, 1999).
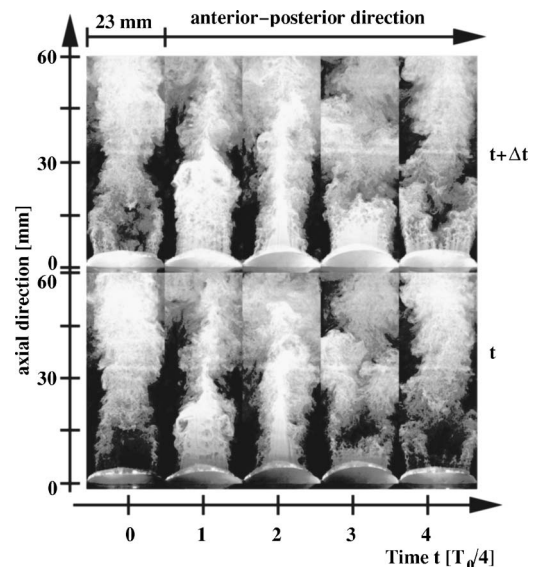
FIG. 10. Three-dimensional features estimated with flow visualization with LASER sheet aligned in anterior-posterior direction. One oscillation cycle of the quasi-phase-locked flow fields is shown. The jet flapped through the LASER sheet in medial-lateral direction and the jet axis was slightly inclined towards one side of the physical model. Hence, at certain parts of the glottal jet the light sheet did not intersect the seeded jet flow. ($\Delta t = 0.5$ ms, $f_{rep} = 15$ Hz, $f_0 = f_{rep}(n+1/N_T) = 123.75$ Hz, with $N_T = 4$ and $n = 8$, volume flow rate: 1050 ml/s, inflow tube length: 81 cm, physical model length: 2.3 cm).

Neubauer *et al.*: Coherent structures of the glottal nearfield

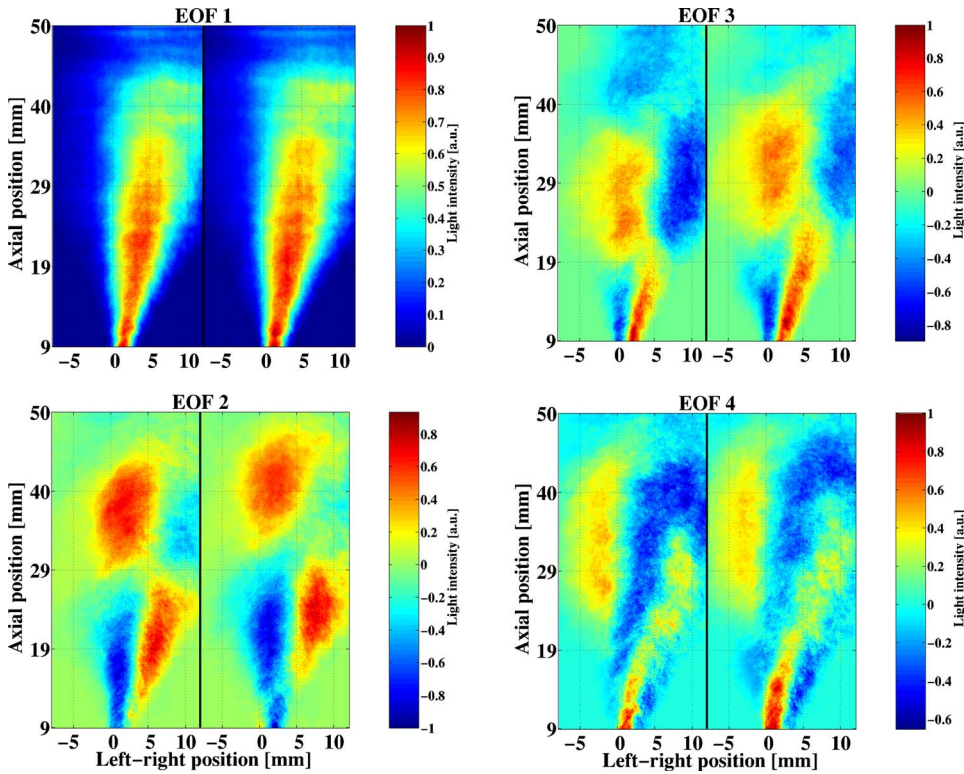FIG. 11. (Color online) First four spatial coherent structures (topos) of the seeding concentration field from paired visualization images downstream from the oscillating physical model. The decomposition into coherent structures of paired images was similar to the decomposition of the flow velocity field of the glottal near field. The disparity of the image pairs of each topos contained the information about the underlying velocity field. Note that EOFs 2 and 3 (and EOFs 4 and 5 (not shown)) are approx. spatially shifted versions of each other. Thus, EOFs 2 and 3 (and EOFs 4 and 5) described traveling wave structures in the seeding concentration field.

E. Linear correlations between laminar core and turbulent region dynamics

1. Coherent structures from seeding concentration fields

We used PCA to objectively extract patterns of correlated flow behavior of the seeding density field in the laminar core region and the turbulent region. In this way, coherent structures were constructed by PCA by finding organized correlated behavior of flow structures.

The snapshot method was used to construct coherent flow structures (in terms of empirical orthogonal functions, EOFs). We used 51 image pairs of seeding concentration fields obtained with double-pulsed light sheet illuminations of the near field of the glottal jet flow. These 51 image pairs captured about seven cycles of the model vibration, similar to the one shown in Fig. 7. Before applying PCA we excluded the downstream protruding superior part of the physical models from the image pairs. In this way, we suppressed the influence of coherent scattered light patterns from the physical model on the construction of coherent flow patterns. The image pairs with a resolution of 800×850 pixels were treated as one image and analyzed together. The disparity between the image pairs is related to the glottal flow velocity field within the light sheet. Therefore, the constructed topos of pairs of seeding concentration fields could be associated with coherent structures of the flow velocity fields downstream from the physical model.

Figure 11 shows the first four spatial coherent structures of image pairs from the seeding concentration field. The corresponding spectra of the chronos are shown in Fig. 12 and the relative eigenvalues are given in Table I. Table I shows that some coherent structures (EOFs) appeared roughly in pairs with respect to their relative contributions to the total

variance (total kinetic energy). Paired eigenvalues were observed previously in other applications of PCA, e.g., see Deane *et al.* (1991); Leonardy *et al.* (1996); Ma and Karniadakis (2002); Ma *et al.* (2003); Noack *et al.* (2003). A theoretical explanation for paired eigenvalues from PCA can be found, e.g., in Glegg and Devenport (2001). In brief, for spatio-temporal systems with homogeneous directions (spatially or temporally translationally invariant directions) PCA modes resemble Fourier modes. Therefore, in spatially ideally homogeneous systems two identical PCA eigenvalues would appear (degenerate case) that are related to sine and cosine functions in space and time. Combined appropriately, paired topos and chronos could describe standing and travel-
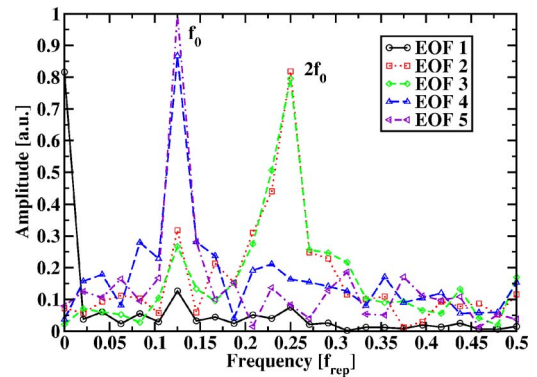
FIG. 12. (Color online) Normalized amplitude spectra of the first five chronos of the coherent structures from the seeding concentration field downstream from the oscillating physical model. The first five chronos could be approximated as: $\varphi_1(t) \propto \text{const.} - \cos(\omega_0 t)$, $\varphi_2(t) \propto \sin(2\omega_0 t)$, $\varphi_3(t) \propto \cos(2\omega_0 t)$, $\varphi_4(t) \propto \sin(\omega_0 t)$, and $\varphi_5(t) \propto \cos(\omega_0 t)$ ($\omega_0 = 2\pi f_0$, $f_{\text{rep}} = 15$ Hz, $f_0 = f_{\text{rep}}(n + f_{\text{exp}}) \approx 122$ Hz, where $f_{\text{exp}} \approx 0.125$ and $n = 8$).

TABLE I. Relative contributions of coherent structures of the near field of the flow visualization experiments to the total kinetic energy, the total mean energy, and the total fluctuating energy. More than 21 components were necessary to explain more than 95% of the total energy. The first component was sufficient to explain more than 95% of the total mean energy, whereas more than 31 components had to be included to recover more than 95% of the total fluctuating energy. ($E_{\text{mean}}/E_{\text{tot}}=43.2\%$, $E_{\text{fluct}}/E_{\text{tot}}=56.8\%$, see Appendix for a theoretical description of these expressions).

PCA index k	Relative contributions of coherent structures to total:		
	kinetic energy $\lambda_k=\langle\Psi_k^2(x)\rangle_x$ [%]	mean energy $\langle\Psi_k(x)\rangle_x^2$ [%]	fluctuating energy $\text{Var}_x(\Psi_k(x))$ [%]
1	76.9	99.6	59.7
2	4.6	$<10^{-1}$	8.0
3	4.1	$<10^{-1}$	7.2
4	1.8	$<10^{-1}$	3.2
5	1.1	$<10^{-1}$	1.9

ing waves. Here, paired eigenvalues of coherent structures were indicative of convection of flow structures in the near field of the glottal jet flow.

The first coherent structure captured approx. 77% of the total kinetic energy, about 100% of the total mean kinetic energy, and 60% of the total fluctuating kinetic energy. The first chronos could be approximated as $\varphi_1(t) \propto \text{const.} - \cos(\omega_0 t)$ ($\omega_0 = 2\pi f_0$, $f_0 \approx 122$ Hz). The first topos could be interpreted as the mean jet flow component that was inclined towards the right model side and oscillated in amplitude at the fundamental frequency of the model vibration.

The second and third coherent structures had similar values for their relative contributions to the total kinetic energy ($\lambda_2 \approx 5\%$, $\lambda_3 \approx 4\%$) and total fluctuating kinetic energy ($\text{Var}_x(\Psi_2(x)) \approx 8\%$, $\text{Var}_x(\Psi_3(x)) \approx 7\%$). Their contributions to the total mean kinetic energy were negligible. The corresponding chronos of these paired coherent structures could be approximated as $\varphi_2(t) \propto \sin(2\omega_0 t)$ and $\varphi_3(t) \propto \cos(2\omega_0 t)$, respectively. Therefore, the dominant frequency component for EOFs 2 and 3 was at the second harmonic ($2\omega_0$). As a pair, EOFs 2 and 3 described the convection of large-scale structures in the turbulent region, as their topos were approx. spatially shifted versions of each other. These two coherent structures showed that the dynamics of flow structures in the right (left) shear layer was strongly correlated with the dynamics of flow structures on the left (right) side of the turbulent region. They captured the correlated motion of the oscillation of the laminar core axis and the jet flapping of the flow in the turbulent region. This interpretation was consistent with our previous observation of the double-peaked behavior of the inclination angle of the laminar core direction (Fig. 6).

The fourth and fifth coherent structures also appeared as a pair with respect to their relative contributions to the total kinetic energy ($\lambda_4 \approx 2\%$, $\lambda_5 \approx 1\%$) and total fluctuating kinetic energy ($\text{Var}_x(\Psi_4(x)) \approx 3\%$, $\text{Var}_x(\Psi_5(x)) \approx 2\%$). Their contributions to the total mean kinetic energy were negligible. Their chronos could be approximated as $\varphi_4(t) \propto \sin(\omega_0 t)$ and $\varphi_5(t) \propto \cos(\omega_0 t)$, with the main frequency component at the fundamental frequency. Their topos (only the topos for the fourth coherent structure is shown here) were again spatially shifted versions of each other. They

showed spatial patterns with three antinodes in the left-right direction compared to two antinodes in left-right direction for the second and third coherent structures. Therefore, they captured smaller-scale details of the oscillation of the laminar core axis and of the flapping of the flow in the turbulent region. Similarly, higher-order coherent structures showed correlated behavior of flow structures on a smaller and smaller spatial scale.

2. Coherent structures from DPIV velocity fields

We used the snapshot method to decompose 50 two-dimensional DPIV velocity fields into coherent flow structures. The field of view for the DPIV observations was about half the size of the flow visualization experiments. In this way, we could focus on the coherent structures only in the immediate downstream near field of the glottal flow. The first four topos are shown in Fig. 13, the magnitude spectra of the corresponding chronos are given in Fig. 14. Table II shows the relative contributions of the coherent structures to the total kinetic energy, the total mean kinetic energy, and the total fluctuating kinetic energy. Similar to the coherent structures found in the seeding density images, coherent structures of the DPIV velocity fields appeared in pairs with respect to their relative contributions to the total kinetic energy. Thus, traveling wave structures, such as convected vortex structures, could be constructed from these paired coherent structures.

The first coherent structure contained about 64% of the total kinetic energy, about 97% of the total mean kinetic energy, and approx. 58% of the total fluctuating kinetic energy. The first topos described the mean jet flow with the mean jet axis inclined towards the right model side. The width of the mean jet flow stayed almost constant over the axial length of about one jet width. Then it widened along the axial direction. The chronos of the first coherent structure showed small amplitude oscillations about a large mean value. Thus, the first coherent structure described a pulsatile mean jet flow downstream from the physical model.

The second coherent structure contained about 8%, 2%, and about 9% of the total kinetic, mean kinetic, and fluctuating kinetic energy, respectively. The corresponding topos showed an antisymmetric velocity field with respect to the
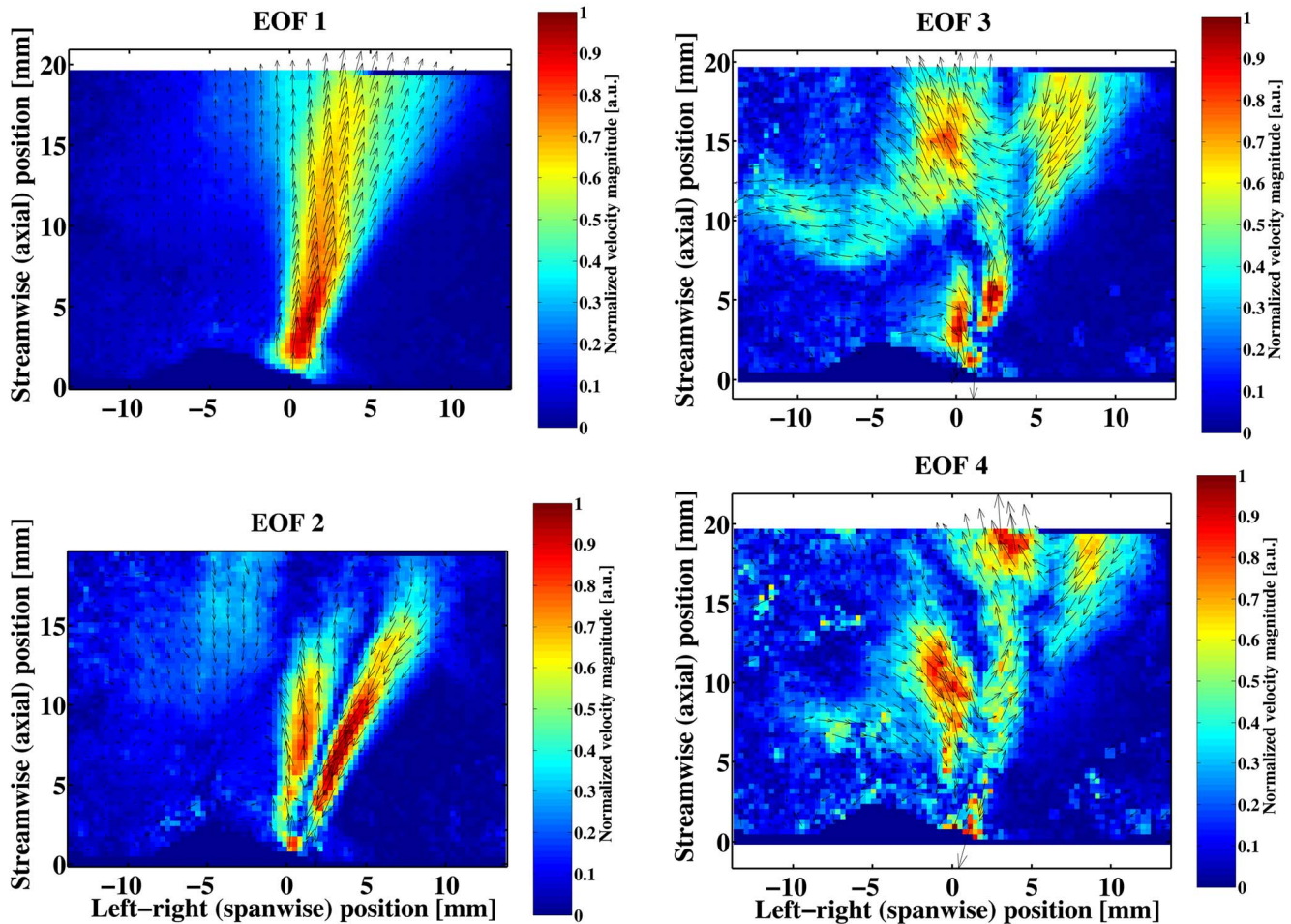
FIG. 13. (Color online) Velocity field and magnitude of the first four topos of the DPIV measurement (every third velocity vector shown): The topos of EOF 1 shows approx. the average velocity field with a mean laminar core width of approx. 2 mm. The topos of EOF 2 captured the left-right oscillation of the jet core location and direction. The topos of EOF 3 and 4 are approx. spatially shifted versions of each other. They showed vortex-like structures convecting downstream. Together, they described the flapping of the jet axis in the turbulent region.

mean jet axis: While the vector field on the left side of the jet core was directed downstream, the vector field on the right jet side was directed upstream (and *vice versa* for the second half of the oscillation cycle). The major frequency component of the corresponding chronos was at the fundamental frequency (f_0) of the model vibration. Therefore, this coherent structure captured the left-right oscillation of the direction of the jet core axis.

The third and fourth coherent structures were approximately spatially shifted versions of each other. They contained about 6% and 2% of the total kinetic energy, and about 7% and 3% of the total fluctuating kinetic energy, respectively. Also the fifth and the sixth coherent structures were spatially shifted versions of each other (not shown here). The topos of EOFs 3 and 4 showed a downstream convecting vortex structure: a vortex-like structure has its center at about $(x,y)=(3,18)$ mm in the topos of EOF 3. The corresponding vortex-like structure can be found at about $(x,y)=(6,21)$ mm in the topos of EOF 4. This vortex rotated in clockwise direction. In the topos of EOF 3, an anti-clockwise rotating vortex-like structure was observed centered at about $(x,y)=(5,5)$ mm downstream from the left side of the model. The major frequency component of the third coherent structure was at the fundamental frequency (f_0). A slightly smaller amplitude was found at the second harmonic ($2f_0$). The fourth coherent structure had its major frequency component at the second harmonic and a slightly weaker component at the fundamental frequency. Thus, the
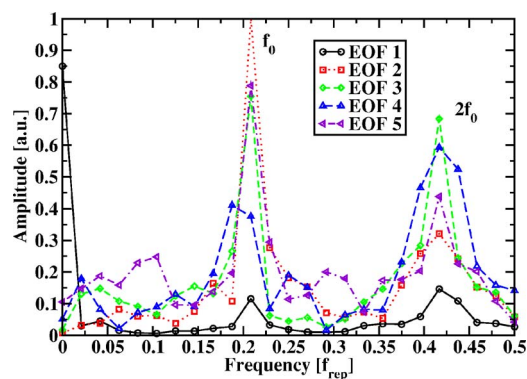

FIG. 14. (Color online) Normalized amplitude spectra of the first five chronos of the velocity field from the DPIV measurement. ($f_0 = (n+f_{exp})f_{rep} \approx 100$ Hz, where $f_{exp} \approx 0.21$, $f_{rep} = 4.95$ Hz and $n=20$).

TABLE II. Relative contributions of coherent structures in the PIV experiments to the total kinetic energy, the total mean energy, and the total fluctuating energy. To recover more than 95% of the total variance of the velocity field, the first 30 EOFs had to be included. The first component was sufficient to explain more than 95% of the total mean energy. More than 32 component had to be included to explain more than 95% of the total fluctuating energy. The total mean energy contains about $E_{mean}/E_{tot}=16.9\%$ of the total kinetic energy, whereas the total fluctuating energy contains about $E_{fluct}/E_{mean}=83.1\%$ of the total energy. (see Appendix for a theoretical description of these expressions).

PCA index k	Relative contributions of coherent structures to total:		
	kinetic energy $\lambda_k=\langle\Psi_k^2(x)\rangle_x$ [%]	mean energy $\langle\Psi_k(x)\rangle_x^2$ [%]	fluctuating energy $\mathrm{Var}_x(\Psi_k(x))$ [%]
1	64.3	96.5	57.8
2	7.7	2.0	8.9
3	6.1	1.2	7.0
4	2.1	$<10^{-1}$	2.6
5	1.4	$<10^{-1}$	1.7
6	1.3	$<10^{-4}$	1.6

third and fourth coherent structures explained the left-right jet flapping in the turbulent region as the convection of vortex structures. They also captured the roll-up of a starting vortex downstream from the left model side.

3. Comparison of coherent structures from seeding concentration fields and DPIV velocity fields

The presented coherent structures from the seeding concentration fields and from the planar DPIV velocity fields were obtained from different sizes of the fields of view: the fields of view for the seeding concentration fields were about twice as large as for the DPIV experiment. Therefore, the DPIV experiment only captured the immediate flow near field downstream from the physical model (the laminar core region, the transitional region, and the beginning of the turbulent region), whereas the flow visualization experiments included a larger part of the turbulent region. Therefore, the coherent structures of the flow visualization experiment captured correlated behavior between the immediate near field and the turbulent region. In this respect, the topos of EOFs 2 and 3 of the flow visualization experiment corresponded to the topos of EOF 2 of the DPIV experiment.

IV. DISCUSSION

In this paper, we used two experimental methods to qualitatively and quantitatively characterize the near field of the glottal flow through a self-sustained oscillating physical model of vocal folds: First, we used the scattered light intensity from a double-pulsed LASER light sheet to qualitatively measure the seeding density field in a single plane of the glottal jet. From the disparity of seeding density patterns of the paired flow visualization images we could estimate the motion of flow patterns. Second, we applied digital particle image velocimetry (DPIV) to quantitatively measure the in-plane flow velocity field in a single plane of the glottal jet.

Due to the limited repetition rate of the double-pulsed LASER we could only obtain a few quasi phase-locked image pairs per glottal jet oscillation. In the future, methods should be developed to increase the number of observable vibration phases. All qualitative and quantitative visualiza-

tion measurements were done for single planes either in axial and left-right direction or in axial and anterior-posterior direction. Thus, we observed that the flow near field is essentially three dimensional. Further experiments have to be done to, first, obtain out-of-plane velocity fields and, second, to get whole-volume measurements of the three-dimensional velocity field of the pulsating glottal jet.

As we used a fairly wide downstream duct (expansion ratio about 127) in our DPIV experiments to increase the seeding density, our DPIV measurements could be considered as open jet experiments. Using DPIV and PCA to extract coherent flow structures from flow velocity fields, future studies could be done on the influence of smaller expansion ratios on the dynamics of the glottal jet. In the human larynx, the ventricular folds could provide such a small expansion ratio. Recently, flow visualization experiments and DPIV measurements with static and driven vocal fold models including the ventricular folds have been reported in Triep *et al.* (2005) and Kucinschi *et al.* (2006).

A. Flow separation and unsteady Coanda effect

1. Asymmetric flow separation inside the glottis

The laminar core axis of the pulsatile glottal jet oscillated in the left-right direction. The jet flow stayed attached at one model side during opening. It then detached and moved to the center of the model glottis while its width increased. During closing, the jet flow reattached to the model side where it was attached during opening. This indicates that the flow separation points within the glottal channel occurred at different axial (inferior-superior) positions on the left and right medial surface of the physical model: The separation points within the glottal channel oscillated in axial direction, and the temporal variation of the jet separation location was different on the left and right model wall. In our experiments, the left and right model sides did not oscillate symmetrically with respect to the medial-lateral and inferior-superior vibration amplitude and phase, although left and right model oscillations were always synchronized to the same fundamental frequency. The asymmetries in amplitude and phase were presumably due to left-right asymmetric

pressure forces related to the asymmetric flow separation points and due to asymmetries in the mounting of the physical models.

We conclude that the flow separation points depended on the detailed instantaneous flow channel geometry. We hypothesize that once the separation points become asymmetric between left and right side, then left-right asymmetric flow pressure forces would act on the glottal channel walls. This would lead to left-right asymmetric vocal fold geometry, even if the visco-elastic vocal fold properties and the initial vocal fold geometry were identical and perfectly symmetric. The asymmetric vocal fold geometry in turn would affect the flow structure, thus completing a flow-structure feedback loop within the glottal channel. Thus, this flow-structure feedback loop inside the glottal channel affects the symmetry of the coupled fluid-structure system. Therefore, this flow-structure feedback could always render the left-right symmetric fluid-structure behavior unstable.

In general, human vocal folds show a similar behavior: Left-right aysmmetries are inherent to the visco-elastic and geometric properties of human vocal folds. However, due to nonlinear coupling (such as from the glottal air stream) human vocal folds typically synchronize to a common fundamental frequency during phonation. For large left-right asymmetries in pathological conditions, such as recurrent nerve paralysis, left and right human vocal folds can disentrain and oscillate at different frequencies (Mergell *et al.*, 2000; Neubauer *et al.*, 2001; Steinecke and Herzel, 1995). Vocal fold asymmetries in healthy normal vocal folds can be induced voluntarily to desynchronize their oscillation. Thus, biphonation and chaotic behavior can be generated by asymmetries (Mergell and Herzel, 1997; Neubauer *et al.*, 2001; Steinecke and Herzel, 1995).

2. Unsteady Coanda effect

We provide further experimental evidence that the 'unsteady Coanda effect' can occur during vocal fold vibration. The term "unsteady Coanda effect" is used in analogy to the "Coanda effect" in stationary flows (Coanda, 1936; Panitz and Wasan, 1972). As our physical model of vocal folds was deformable, the divergence angle of the glottis [corresponds to include angle in Scherer *et al.* (2001); Shinwari *et al.* (2003)] and the glottal channel direction [termed obliquity in Scherer *et al.*, 2001; Shinwari *et al.*, 2003] were dynamic variables, in contrast to previous experiments where they were only control parameters (Erath, 2005; Pelorson *et al.*, 1994; Shinwari *et al.*, 2003; Triep *et al.*, 2005; Vilain *et al.*, 1999). Dynamically, maximum divergence angles typically occurred when the volume flow was maximal. The divergence angles of the left and right model at the downstream side of the model were asymmetric due to the construction of the physical model.

Measurements by Pelorson *et al.* (1994) and Vilain *et al.* (1999) with static and driven vocal fold models and starting or pulsatile flow found that the Coanda effect might not occur during phonation due to its large buildup time compared to the oscillation period. Recently, Erath (2005) and Erath and Plesniak (2006a, b, c) found that the unsteady Coanda effect occurs in pulsatile flows through static glottal channels

with different divergence angles at their outlet. In a recent DPIV study on a driven vocal fold model, Triep *et al.* (2005) found that the unsteady Coanda effect occured during the opening of the driven glottis.

Our observations show that an unsteady Coanda effect can occur under unsteady oscillatory conditions, as we observed attached jet flow to only one model side, predominantly during glottal opening and closing. Our hypothesis is that the unsteady Coanda effect may be induced by flow structures downstream from the vocal folds.

B. Feedback/feedforward mechanisms in the glottal flow

1. Flapping of the turbulent jet region

In our flow visualization experiments, the jet axis in the transition region and the turbulent region showed wavey undulations in axial direction: The jet appeared to be flapping like a flag in the left-right direction. Our flow visualization experiments and DPIV measurements showed that large-scale vortex structures were generated and convected downstream into the transitional and turbulent region. The starting jet flow at the beginning of the oscillation cycle might have initiated the roll-up of these large-scale vortex structures. Note that this roll-up might be also influenced by the remaining flow structures from the previous cycle. The particular spatial alignment of large-scale vortex structures would result in an apparent flapping motion of the seeded jet flow. Analogous to planar jet experiments (Gordeyev and Thomas, 2000; Thomas and Brehob, 1986; Thomas and Prakash, 1991), we note that the term flapping jet is a misnomer in the context of glottal jets. We propose that the glottal jet axis in the turbulent region is undulated due to antisymmetric large-scale vortex structures that are convected downstream. Therefore, at a fixed axial position the jet axis appears to be oscillating in the left-right direction. Applying PCA to flow visualization fields and DPIV velocity fields, we found paired coherent structures that indicated sine and cosine-like flow patterns in the axial direction. The superposition of these patterns explained the flapping turbulent jet similar to a traveling wave. This corroborated our hypothesis that flapping was caused by convecting vortex structures in the transitional and turbulent region.

2. Coherent structures reveal correlations of the laminar core region and the turbulent region

Coherent flow structures were extracted from the near field flow. By construction from PCA, coherent flow structures revealed spatio-temporal patterns that showed correlated flow motion of the laminar core region, the surrounding shear layer, and the turbulent region. Coherent, i.e., correlated behavior might indicate a coupling mechanism, a "feedback/feedforward coupling" of the glottal flow and its downstream near field. Such a feedback/feedforward coupling of the shear layer mode with the jet column mode (i.e., the large-scale vortices in the transitional and turbulent region), has been found previously in planar jet experiments. In analogy to these planar jet experiments through static planar orifices (Huang and Hsiao, 1999; Thomas and Chu,

1989; Thomas and Prakash, 1991), it is possible that the free shear layers around the laminar core region and the boundary layers within the glottis may be strongly influenced by an acoustic and hydrodynamic interaction with the roll-up of large-scale vortex rings. Such a mechanism was already discussed by McGowan (1988).

Based on our extracted coherent flow structures, we hypothesize that there could be different mechanisms that could induce left-right asymmetric fluid-structure oscillatory behavior in oscillating physical models. Highly correlated regions within the first few dominant coherent structures were located on opposite sides of the axial jet centerline: The left (right) shear layer dynamics was positively correlated to the dynamics of the right (left) turbulent region. This observation may indicate that pulsatile glottal jets may be dynamically similar to planar jets (Gordeyev and Thomas, 2000; Thomas and Brehob, 1986; Thomas and Prakash, 1991). Spatial correlations in planar jets from symmetric static slit-like orifices explaining jet flapping (Thomas and Chu, 1989; Thomas and Prakash, 1991) were similar to the coherent structures observed in our physical model.

This dynamic similarity would imply that an interaction mechanism exists in pulsatile glottal jets that couples the shear layers around the laminar core region with the roll-up of large-scale vortices in the transition region. Thus, jet flapping in the turbulent region would be coupled with the shear layer dynamics (i.e., the shear layer mode). As explained above, jet flapping could be explained by an antisymmetric staggered array of large-scale vortex structures in the turbulent region. In analogy to static planar jet experiments (Thomas and Chu, 1989; Thomas and Prakash, 1991), we use the term "jet column mode" for this flow structure.

The buildup of this jet column mode in the transitional region could create an acoustic dipole due the vortex generation in the transition region. Following Thomas and Prakash (1991), the pressure waves from this dipole could disturb the shear layer mode (i.e., the von Kármán-like vortex street) close to the glottal discharge plane (feedback mechanism). In turn, disturbances of the shear layers would convect downstream until they would reach the transitional region to affect the vortex generation (feedforward mechanism).

Furthermore, the shear layers could affect the flow separation points in the glottis (feedback mechanism). Hence, the unsteady Coanda effect (i.e., asymmetric flow separation locations) discussed above might be even induced by the feedback interaction of the jet column mode with the shear layer mode. Disturbances in the shear layer might affect the boundary layers in the glottis. Thus, this might help to break the symmetry of the flow in the glottal channel. In turn, this might again influence the jet column mode and the flapping jet. Overall, this might close a feedback/feedforward loop comprising the glottal wall geometry (and the glottal viscoelastic properties), the flow pressure distribution in the glottal channel, and the near field of the glottal jet. Hence, the glottal dynamics would not only be affected by the flow in the glottal channel, but also by the near field of the glottal jet. Future experiments should further explore this hypothesis.

3. Influence of acoustic pressure field on glottal jet structures and dynamics

When the glottis is open, the glottal jet could be affected by the acoustic pressure in the subglottal, upstream system. It has been shown that the coherent structures of acoustically excited jets through static orifices behave different from "natural" unexcited jets (Faghani et al., 1999; Kang et al., 1998; Olsen et al., 2003; Schram et al., 2005; Thomas and Brehob, 1986; Thomas and Chu, 1989; Thomas and Prakash, 1991; Zhao et al., 2001). Confined jets through static orifices can also be affected by the downstream acoustics. Maurel et al. (1996) showed that the downstream cavity length facilitated self-sustained jet oscillations (jet flapping) at a frequency determined by the cavity length. Studies on forced jets (e.g., Hsiao and Huang, 1990a, b; Huang and Hsiao, 1999; Peacock et al., 2004) showed that oscillations of the jet orifice walls or acoustic pressure fluctuations at the trailing edge of the nozzle can control the symmetry of the instability mode in the shear layer around the laminar core region. Symmetric and antisymmetric modes could be selected using different oscillation frequencies of the orifice wall or acoustic pressure disturbance at the trailing edge of the nozzle. Moreover, the dynamics of the turbulent jet region can be affected by such acoustic or mechanic excitations of the shear layers in the laminar core region (Reynolds et al., 2003).

C. Reduced-order dynamic models for glottal fluid-structure oscillator

Our study could be regarded as an extension of the work by Shinwari et al. (2003). In particular, they used flow visualization to qualitatively study the steady glottal jet flow through static glottal models. They used divergent glottal channel geometries that were either left-right symmetric or oblique (asymmetric). In two schematic drawings they qualitatively sketched the coherent flow structures of the flow near field downstream from the flow separation points. Here, we used PCA to quantify coherent flow patterns found in our self-sustained oscillating physical model. We also propose that in studies with static glottal models, coherent structures in terms of empirical orthogonal eigenfunctions should be extracted with PCA. This approach would allow a quantitative comparison of the flow structures found in experiments with static and self-sustained oscillating models.

More important, relevant mechanisms for the interaction of the glottal near field with the intraglottal flow can be parameterized using coherent flow structures: Reduced-order models can be constructed by "projecting" the governing equations of fluid dynamics onto a dynamically dominant subset of empirical coherent structures. This approach, sometimes called the "empirical Galerkin method" (Lumley and Blossey, 1998; Noack et al., 2004), has been used in classical systems in unsteady fluid dynamics, e.g., cylinder wake flow (Ma and Karniadakis, 2002; Ma et al., 2003; Noack et al., 2003; Sirisup et al., 2004), airfoils (Dowell and Hall, 2001), and two-dimensional unsteady flows in complex geometries (Deane et al., 1991). Therefore, coherent structures could

facilitate the development of reduced-order dynamic models of the near field flow in static, driven, and self-sustained oscillating models of vocal fold vibration.

D. Interpretation of two-dimensional flow field representations

In this paper we presented two-dimensional velocity field measurements of a pulsatile glottal jet. We used measurement planes that intersected the glottal jet in different directions. Therefore, we showed that the glottal jet downstream from a physical model of vocal folds has an inherently three-dimensional structure. We found that the glottal flow near field of a self-sustained oscillating model of vocal folds was essentially three-dimensional and unsteady (time dependent). Caution has to be taken in the interpretations of two-dimensional flow visualization experiments where the time-dependent flow field images represent only two-dimensional slices of the flow. Azimuthal structures with out-of-plane motion and therefore three-dimensional effects were neglected in our study. For regular vocal fold oscillations, traversing measurement planes in future experiments could resolve the dynamics of the glottal jet in different layers. Thus, three-dimensional coherent flow structures could be observed. New developments in high speed DPIV (e.g., tomographic DPIV) would allow to also study glottal jets during nonstationary and irregular vocal fold oscillations. This would be especially important to further understand pathological voice production.

E. Interpretation of seeding density fields

Flow visualization measurements should be interpreted with caution, as the images only represent concentration fields of the seeding particles and the dynamics of the underlying velocity and pressure fields are unknown. If the seeding density is high as in our experiments, only the boundaries between the seeded glottal flow and the unseeded surrounding air could be detected in the near field. Therefore, the classic Kelvin-Helmholtz roll-up of the shear layers resulting in von Kármán-like vortex streets could be visually observed (Winter *et al.* (1987)). Flow visualization might not be able to show staggered vortex arrays in the transitional and turbulent region, as the seeding particles diffuse too fast for any discrete vortical structures to be visible after some distance downstream from the glottis. Nevertheless, Kirby *et al.* (1990) and Sirovich *et al.* (1990) showed that concentration field patterns can still be interpreted in terms of the actual fluid motion. Kirby *et al.* (1990) used computer simulations of steady open jet flows to compare the coherent structures (in terms of EOFs) from the flow velocity and pressure fields with the EOFs from the corresponding mass fraction field. The mass fraction is related to the seeding density and thus the scattered light intensity captured in flow visualization experiments. They showed that principal component analysis of the mass fraction field still yielded qualitatively similar information about the coherent flow patterns.

F. Preliminary studies and directions for future research

Using a physical rubber model of vocal folds, we showed the existence of coherent structures in this artificial glottal jet. In preliminary experiments on excised human and canine larynges we confirmed the existence of a flapping jet structure and of the left-right oscillation of the laminar core. The presented experiments on the jet flow through a physical model of vocal folds appeared to be qualitatively similar to these preliminary observations. Future work with excised larynx preparations using the presented experimental and analytical techniques should explore this behavior further.

V. CONCLUSION

Using methods of flow visualization and digital particle image velocimetry (DPIV), this study measured the near field flow structures immediately downstream of a self-oscillating, physical model of the vocal folds, with a vocal tract attached. A spatio-temporal analysis of the structures was performed using the method of empirical orthogonal eigenfunctions. Some of the observed flow structures included vortex generation, vortex convection, and jet flapping. Jet flapping was observed, presumably due to antisymmetric (staggered) arrays of large-scale vortices in the streamwise direction in the turbulent region. In the transition region of the glottal jet, large-scale vortices were generated, presumably from the growing instability waves in the free shear layer surrounding the laminar core region. It is hoped that this paper will stimulate the development of low-order models, as well as more detailed experiments regarding the interaction of coherent structures with each other and the vibrating vocal folds.

APPENDIX: COHERENT STRUCTURES CONSTRUCTED FROM PRINCIPAL COMPONENT ANALYSIS (PCA)

Principal component analysis (PCA) was used to extract mutually decorrelated (orthogonal) spatio-temporal structures from measured complex spatio-temporal flow velocity fields $\mathbf{V}(\mathbf{x}, t)$, $\mathbf{x} \in \mathbb{R}^2$, $t \in \mathbb{R}$. PCA is also commonly referred to as "empirical orthogonal function analysis," "biorthogonal decomposition," "Karhunen-Loéve expansion," "proper orthogonal decomposition," "principal factor analysis," "singular value analysis," and the "singular spectrum analysis" (Berry *et al.*, 1994). Consider the discretized velocity field "movie" $\mathbf{V}(x_k, y_\ell, t_i)$ describing the measured spatio-

temporal velocity field. Here, x_k, $k=1,\ldots,N_x$, y_l, $l=1,\ldots,N_y$, indicate the spatial coordinates (in left-right and anterior-posterior direction), and t_i, $i=1,\ldots,M$ is the time index. We used the "snapshot method" (Sirovich, 1987) to analyze the spatio-temporal flow velocity fields obtained from flow visualization and digital particle image velocimetry (DPIV). The covariance matrix $\mathbf{K}$ measures linear correlations of the velocity field $\mathbf{V}(x_k,y_l,t_i)$ by comparing on average the behavior of the measured field variable at all different measured time instances (snapshots) t_i:

$$K(t_k,t_\ell) = \frac{1}{N}\sum_{i=1}^{N} \mathbf{V}(\mathbf{x}_i,t_k)\cdot\mathbf{V}(\mathbf{x}_i,t_\ell) = \langle \mathbf{V}(\mathbf{x}_i,t_k)\cdot\mathbf{V}(\mathbf{x}_i,t_\ell)\rangle_{\mathbf{x}_i} \quad (A1)$$

with k, $l=1,\ldots,M$ and $N=N_x*N_y$. The symbol $\langle\cdot\rangle_{\mathbf{x}_i}$ denotes a spatial average. We do not exclude the spatial or the temporal mean of the velocity field $\mathbf{V}(x_k,y_l,t_i)$ before calculating the covariance matrix, as this would introduce artificial correlations to the measured spatio-temporal field (Aubry *et al.*, 1991). The covariance matrix is a real, symmetric and positive semidefinite matrix. Therefore, it can be diagonalized and has real and non-negative eigenvalues:

$$\mathbf{K}\varphi_\ell = \lambda_\ell\varphi_\ell. \quad (A2)$$

The normalized eigenvectors $\varphi_l(t)$, $l=1,\ldots,M$, correspond to the empirical orthogonal functions (EOFs). Sometimes they are called "chronos" to indicate their chronological meaning (Aubry *et al.*, 1991). The eigenvalues λ_l are the "weights" of the normalized EOFs. They reflect the contributions of the EOFs to the overall variance. The eigenfunctions define a set of orthogonal directions in the 2M-dimensional state space $\{\mathbf{V}(t_l)\}$, and the eigenvalues are the variances of the measured velocity field movie $\mathbf{V}(\mathbf{x},t)$ projected onto the EOF directions. The eigenfunctions are sorted with respect to their variances.

The total variance E_{tot} (total kinetic energy (Aubry *et al.*, 1991)) of the set of states $\{\mathbf{V}(\mathbf{x}_k,t_i)\}$ is given by the sum of the eigenvalues λ_l:

$$E_{\text{tot}} = \sum_{\ell=1}^{N}\lambda_\ell = \langle\mathbf{V}(\mathbf{x}_k,t_i)\cdot\mathbf{V}(\mathbf{x}_k,t_i)\rangle_{\mathbf{x}_k,t_i}, \quad (A3)$$

where λ_l is the variance of one single spatio-temporal structure. As the EOFs φ_l establish an ortho-normal system $(\langle\varphi_k(t)\varphi_l(t)\rangle_t=\delta_{kl})$, the "movie" $\mathbf{V}(\mathbf{x}_k,t_i)$ can be written as a linear superposition:

$$\mathbf{V}(\mathbf{x}_k,t_i) = \sum_{\ell=1}^{M}\mathbf{\Psi}_\ell(\mathbf{x}_k)\varphi_\ell(t_i). \quad (A4)$$

The spatial expansion coefficients $\mathbf{\Psi}_l(\mathbf{x}_i)$ are determined by the projection of the movie onto the eigenfunctions:

$$\mathbf{\Psi}_\ell(\mathbf{x}_i) = \sum_{k=1}^{M}\mathbf{V}(\mathbf{x}_i,t_k)\varphi_\ell(t_k) = \langle\mathbf{V}(\mathbf{x}_i,t)\varphi_\ell(t)\rangle_t. \quad (A5)$$

Sometimes, the spatial coefficients are called "topos," as they express the topological importance of the associated chronos (Aubry *et al.*, 1991). They also can be regarded as

spatial eigenfunctions corresponding to their associated chronos that can be thought of as temporal eigenfunctions. Finally, the velocity field movie can be decomposed as

$$\mathbf{V}(\mathbf{x}_k,t_i) = \sum_{\ell=1}^{M}\sigma_\ell\boldsymbol{\psi}_\ell(\mathbf{x}_k)\varphi_\ell(t_i) \quad (A6)$$

with $\boldsymbol{\psi}_l(\mathbf{x}_k)$ defined as

$$\mathbf{\Psi}_\ell(\mathbf{x}_k) = \sigma_\ell\boldsymbol{\psi}_\ell(\mathbf{x}_k), \quad (A7)$$

$$\sigma_\ell = \sqrt{\lambda_\ell}. \quad (A8)$$

Here, we used the following:

$$\langle\mathbf{\Psi}_k(\mathbf{x}_i)\cdot\mathbf{\Psi}_\ell(\mathbf{x}_i)\rangle_{\mathbf{x}_i} = \lambda_k\delta_{k\ell} = \sigma_k\sigma_\ell\langle\boldsymbol{\psi}_k(\mathbf{x}_i)\cdot\boldsymbol{\psi}_\ell(\mathbf{x}_i)\rangle_{\mathbf{x}_i}. \quad (A9)$$

Thus, the normalized topos $\boldsymbol{\psi}_l(\mathbf{x}_i)$ also establish an ortho-normal system of empirical spatial eigenfunctions.

Another useful property of the topos $\boldsymbol{\psi}_k(\mathbf{x}_i)$ and the weights (total kinetic energy) λ_k can be derived using the general relationship between the variance of a function $\mathbf{f}(x)$ and its first two moments:

$$\text{Var}_x(\mathbf{f}(x)) = \langle(\mathbf{f} - \langle\mathbf{f}\rangle_x)^2\rangle_x = \langle\mathbf{f}^2\rangle_x - \langle\mathbf{f}\rangle_x^2. \quad (A10)$$

Therefore, we can write

$$\text{Var}_\mathbf{x}(\mathbf{\Psi}_k(\mathbf{x})) = \langle\mathbf{\Psi}_k^2(\mathbf{x})\rangle_\mathbf{x} - \langle\mathbf{\Psi}_k(\mathbf{x})\rangle_\mathbf{x}^2. \quad (A11)$$

Together with $\langle\mathbf{\Psi}_k(\mathbf{x})\cdot\mathbf{\Psi}_l(\mathbf{x})\rangle_\mathbf{x}=\lambda_k\delta_{kl}$, we arrive at

$$\lambda_k = \langle\mathbf{\Psi}_k(\mathbf{x})\rangle_\mathbf{x}^2 + \text{Var}_\mathbf{x}(\mathbf{\Psi}_k(\mathbf{x})). \quad (A12)$$

With $E_{\text{tot}}=\langle\mathbf{V}(\mathbf{x}_k,t_i)\cdot\mathbf{V}(\mathbf{x}_k,t_i)\rangle_{\mathbf{x}_k,t_i}=\Sigma_{k=1}^{M}\lambda_k$ for the total kinetic energy, we can further write

$$E_{\text{tot}} = \sum_{k=1}^{M}\langle\mathbf{\Psi}_k(\mathbf{x})\rangle_\mathbf{x}^2 + \sum_{k=1}^{M}\text{Var}_\mathbf{x}(\mathbf{\Psi}_k(\mathbf{x})) = E_{\text{mean}} + E_{\text{fluct}} \quad (A13)$$

Thus, the contribution λ_k/E_{tot} of each EOF $\varphi_k(t)$ (chronos) to the total variance (the total kinetic energy) of the spatio-temporal velocity field movie $\mathbf{V}(\mathbf{x},t)$ can be separated into the contribution to the total mean kinetic energy $\langle\mathbf{\Psi}_k(\mathbf{x})\rangle_\mathbf{x}^2/E_{\text{mean}}$ and to the total fluctuating kinetic energy $\text{Var}_\mathbf{x}(\mathbf{\Psi}_k(\mathbf{x}))/E_{\text{fluct}}$.

$$\sum_{k=1}^{M}\frac{\lambda_k}{E_{\text{tot}}} = \frac{E_{\text{mean}}}{E_{\text{tot}}}\sum_{k=1}^{M}\langle\mathbf{\Psi}_k(\mathbf{x})\rangle_\mathbf{x}^2/E_{\text{mean}}$$

$$+ \frac{E_{\text{fluct}}}{E_{\text{tot}}}\sum_{k=1}^{M}\text{Var}_\mathbf{x}(\mathbf{\Psi}_k(\mathbf{x}))/E_{\text{fluct}}. \quad (A14)$$

Adrian, R. J. (**1991**). "Particle-imaging techniques for experimental fluid mechanics," Annu. Rev. Fluid Mech. **23**, 261–304.

Aubry, N., Guyonnet, R., and Lima, R. (**1991**). "Spatiotemporal analysis of complex signals: Theory and application," J. Stat. Phys. **64**, 683–739.

Barney, A., Shadle, C. H., and Davies, P. O. A. L. (**1999**). "Fluid flow in a dynamic mechanical model of the vocal folds and tract. I. Measurements and theory," J. Acoust. Soc. Am. **105**, 444–455.

Berkooz, G., Holmes, P., and Lumley, J. L. (**1993**). "The proper orthogonal decomposition in the analysis of turbulent flows," Annu. Rev. Fluid Mech. **25**, 539–575.

Berry, D. A., Herzel, H., Titze, I. R., and Krischer, K. (**1994**). "Interpretation of biomechanical simulations of normal and chaotic vocal fold oscillations with empirical eigenfunctions," J. Acoust. Soc. Am. **95**, 3595–3604.

Coanda, H. (**1936**). "Device for deflecting a stream of elastic fluid projected into an elastic fluid," U.S. Patent No. 2,052,869, Sept. 1.

Deane, A. E., Kevrekidis, I. G., Karniadakis, G. E., and Orszag, S. A. (**1991**). "Low-dimensional models for complex geometry flows: Application to grooved channels and circular cylinders," Phys. Fluids **3**, 2337–2354.

Dowell, E. H., and Hall, K. C. (**2001**). "Modeling of fluid-structure interaction," Annu. Rev. Fluid Mech. **33**, 445–490.

Erath, B. D. (**2005**). *An Experimental Investigation of Velocity Fields in Divergent Glottal Models of the Human Vocal Tract*, Master's thesis, Purdue University.

Erath, B. D., and Plesniak, M. W. (**2006a**). "An investigation of bimodal jet trajectory in flow through scaled models of the human vocal tract," Exp. Fluids **40**, 683–696.

Erath, B. D., and Plesniak, M. W. (**2006b**). "An investigation of jet trajectory in flow through scaled vocal fold models with asymmetric glottal passages," Exp. Fluids **41**, 735–748.

Erath, B. D., and Plesniak, M. W. (**2006c**). "The occurrence of the Coanda effect in pulsatile flow through static models of the human vocal folds," J. Acoust. Soc. Am. **120**, 1000–1011.

Faghani, D., Sévrain, A., and Boisson, H.-C. (**1999**). "Physical eddy recovery through bi-orthogonal decomposition in an acoustically forced plane jet," Flow, Turbul. Combust. **62**, 69–88.

Fant, G. (**1960**). *Acoustic Theory of Speech Production* (Hague Mouton, The Netherlands).

Glegg, S. A. L., and Devenport, W. J. (**2001**). "Proper orthogonal decomposition of turbulent flows for aeroacoustic and hydroacoustic applications," J. Sound Vib. **239**, 767–784.

Gordeyev, S. V., and Thomas, F. O. (**2000**). "Coherent structure in the turbulent planar jet. Part 1. Extraction of proper orthogonal decomposition eigenmodes and their self-similarity," J. Fluid Mech. **414**, 145–194.

Gutmark, E. J., and Grinstein, F. F. (**1999**). "Flow control with noncircular jets," Annu. Rev. Fluid Mech. **31**, 239–272.

Hirschberg, A. (**1992**). "Some fluid dynamic aspects of speech," Bulletin de la Communication Parlée **2**, 7–30.

Hirschberg, A., Pelorson, X., Hofmans, G., van Hassel, R. R., and Wijnands, A. P. J. (**1996**). "Starting transient of the flow through an in-vitro model of the vocal folds," in *Vocal Fold Physiology: Controlling Complexity and Chaos*, edited by P. J. Davies, and P. J. Fletcher (Singular, San Diego), pp. 31–46.

Hofmans, G. C. J. (**1998**). *Vortex Sound in Confined Flows*, Ph.D. thesis, Technische Universiteit Eindhoven, The Netherlands.

Hofmans, G. C. J., Boot, R. J. J., Durrieu, P. P. J. M., Auregan, Y., and Hirschberg, A. (**2001a**). "Aeroacoustic response of a slit-shaped diaphragm in a pipe at low Helmholtz number, 1: Quasi-steady results," J. Sound Vib. **244**, 35–56.

Hofmans, G. C. J., Groot, G., Ranucci, M., Graziani, G., and Hirschberg, A. (**2003**). "Unsteady flow through in-vitro models of the glottis," J. Acoust. Soc. Am. **113**, 1658–1675.

Hofmans, G. C. J., Ranucci, M., Ajello, G., Auregan, Y., and Hirschberg, A. (**2001b**). "Aeroacoustic response of a slit-shaped diaphragm in a pipe at low Helmholtz number, 2: Unsteady results," J. Sound Vib. **244**, 57–77.

Holmes, J. D., Lumley, J. L., and Berkooz, G. (**1996**). *Turbulence, Coherent Structures and Symmetry* (Cambridge University Press, Cambridge, UK).

Holmes, P. J., Lumley, J. L., Berkooz, G., Mattingly, J. C., and Wittenberg, R. W. (**1997**). "Low-dimensional models of coherent structures in turbulence," Phys. Rep. **287**, 337–384.

Howe, M. S., and McGowan, R. S. (**2005**). "Aeroacoustics of [s]," Proc. R. Soc. London, Ser. A **461**, 1005–1028.

Hsiao, F.-B., and Huang, J.-M. (**1990a**). "Near-field flow structures and sideband instabilities of an initially laminar plane jet," Exp. Fluids **9**, 2–12.

Hsiao, F.-B., and Huang, J.-M. (**1990b**). "On the evolution of instabilities in the near field of a plane jet," Phys. Fluids A **2**, 400–412.

Huang, J.-M., and Hsiao, F.-B. (**1999**). "On the mode development in the developing region of a plane jet," Phys. Fluids **11**, 1847–1857.

Kang, Y., Karagozian, A. R., and Smith, O. I. (**1998**). "Transport enhancement in acoustically excited cavity flows, part 1: Nonreactive flow diagnostics," AIAA J. **36**, 1562–1567.

Kirby, M., Boris, J., and Sirovich, L. (**1990**). "An eigenfunction analysis of axisymmetric jet flow," J. Comput. Phys. **90**, 98–122.

Krane, M. H. (**2005**). "Aeroacoustic production of low-frequency unvoiced speech sounds," J. Acoust. Soc. Am. **118**, 410–427.

Kucinschi, B. R., Scherer, R. C., DeWitt, K. J., and Ng, T. T. M. (**2006**). "Flow visualization and acoustic consequences of the air moving through a static model of the human larynx," J. Biomater. Appl. **128**, 380–390.

Leonardy, J., Kaiser, F., Belić, M. R., and Hess, O. (**1996**). "Running transverse waves in optical phase conjugation," Phys. Rev. A **53**, 4519–4527.

Lumley, J., and Blossey, P. (**1998**). "Control of turbulence," Annu. Rev. Fluid Mech. **30**, 311–327.

Lumley, J. L. (**1967**). "The structure of inhomogeneous turbulent flows," in *Atmospheric Turbulence and Radio Wave Wave Propagation*, edited by A. M. Yaglom, and V. I. Tatarski (Nauka, Moscow), pp. 166–178.

Ma, X., and Karniadakis, G. E. (**2002**). "A low-dimensional model for simulating three-dimensional cylinder flow," J. Fluid Mech. **458**, 181–190.

Ma, X., Karniadakis, G. E., Park, H., and Gharib, M. (**2003**). "DPIV-driven flow simulation: A new computational paradigm," Proc. R. Soc. London, Ser. A **459**, 547–565.

Maurel, A., Ern, P., Zielinska, B. J. A., and Wesfreid, J. E. (**1996**). "Experimental study of self-sustained oscillations in a confined jet," Phys. Rev. E **54**, 3643–3651.

McGowan, R. S. (**1988**). "An aeroacoustic approach to phonation," J. Acoust. Soc. Am. **83**, 696–704.

McGowan, R. S., and Howe, M. S. (2006). "Compact Green's functions extend the acoustic theory of speech production," J. Phonetics (in press).

Mergell, P., and Herzel, H. (**1997**). "Modelling biphonation-the role of the vocal tract," Speech Commun. **22**, 141–154.

Mergell, P., Herzel, H., and Titze, I. R. (**2000**). "Irregular vocal fold vibration—High-speed observation and modeling," J. Acoust. Soc. Am. **108**, 2996–3002.

Neubauer, J., Mergell, P., Eysholdt, U., and Herzel, H. (**2001**). "Spatio-temporal analysis of irregular vocal fold oscillations: Biphonation due to desynchronization of spatial modes," J. Acoust. Soc. Am. **110**, 3179–3192.

Noack, B. R., Afanasiev, K., Morzynski, M., Tadmor, G., and Thiele, F. (**2003**). "A hierarchy of low-dimensional models for the transient and post-transient cylinder wake," J. Fluid Mech. **497**, 335–363.

Noack, B. R., Tadmor, G., and Morzyński, M. (**2004**). "Low-dimensional models for feedback flow control. Part I: Empirical Galerkin models," in *Second AIAA Flow Control Conference*, Portland, OR, p. 2408.

Olsen, J. F., Rajagopalan, S., and Antonia, R. A. (**2003**). "Jet column modes in both a plane jet and a passively modified plane jet subject to acoustic excitation," Exp. Fluids **35**, 278–287.

Panitz, T., and Wasan, D. T. (**1972**). "Flow attachment to solid surfaces: The Coanda effect," AIChE J. **18**, 51–57.

Peacock, T., Bradley, E., Hertzberg, J., and Lee, Y.-C. (**2004**). "Forcing a planar jet flow using MEMS," Exp. Fluids **37**, 22–28.

Pelorson, X., Hirschberg, A., van Hassel, R. R., and Wijnands, A. P. J. (**1994**). "Theoretical and experimental study of quasisteady-flow separation within the glottis during phonation. Application to a modified two-mass model," J. Acoust. Soc. Am. **96**, 3416–3431.

Reynolds, W. C., Parekh, D. E., Juvet, P. J. D., and Lee, M. J. D. (**2003**). "Bifurcating and blooming jets," Annu. Rev. Fluid Mech. **35**, 295–315.

Scherer, R. C., Shinwari, D., Witt, K. J. D., Zhang, C., Kucinschi, B. R., and Afjeh, A. A. (**2001**). "Intraglottal pressure profiles for a symmetric and oblique glottis with a divergence angle of 10 degrees," J. Acoust. Soc. Am. **109**, 1616–1630.

Schram, C., Taubnitz, S., Anthoine, J., and Hirschberg, A. (**2005**). "Theoretical/empirical prediction and measurement of the sound produced by vortex pairing in a low Mach number jet," J. Sound Vib. **281**, 171–187.

Shadle, C. H., Barney, A., and Davies, P. O. A. L. (**1999**). "Fluid flow in a dynamic mechanical model of the vocal folds and tract: II. Implications for speech production studies," J. Acoust. Soc. Am. **105**, 456–466.

Shinwari, D., Scherer, R. C., DeWitt, K. J., and Afjeh, A. A. (**2003**). "Flow visualization and pressure distributions in a model of the glottis with a symmetric and oblique divergent angle of 10 degrees," J. Acoust. Soc. Am. **113**, 487–497.

Sirisup, S., Karniadakis, G. E., Yang, Y., and Rockwell, D. (**2004**). "Wave-structure interaction: Simulation driven by quantitative imaging," Proc. R. Soc. London, Ser. A **460**, 729–755.

Sirovich, L. (**1987**). "Turbulence and the dynamics of coherent structures. I—Coherent structures. II—Symmetries and transformations. III—Dynamics and scaling," Q. Appl. Math. **45**, 561–571.

Sirovich, L., Kirby, M., and Winter, M. (**1990**). "An eigenfunction approach

J. Acoust. Soc. Am., Vol. 121, No. 2, February 2007

Neubauer *et al.*: Coherent structures of the glottal nearfield   1117

to large scale transitional structures in jet flow," Phys. Fluids A **2**, 127–136.

Steinecke, I., and Herzel, H. (**1995**). "Bifurcations in an asymmetric vocal fold model," J. Acoust. Soc. Am. **97**, 1571–1578.

Stevens, K. N. (**1998**). *Acoustic Phonetics* (MIT Press, Cambridge, MA).

Theodorsen, T. (**1952**). "Mechanism of turbulence," in *Second Midwestern Conference on Fluid Mechanics* (Ohio State University, Columbus, OH).

Thomas, F. O., and Brehob, E. G. (**1986**). "An investigation of large-scale structure in the similarity region of a two-dimensional turbulent jet," Phys. Fluids **29**, 1788–1795.

Thomas, F. O., and Chu, H. C. (**1989**). "An experimental investigation of the transition of a planar jet: Subharmonic suppression and upstream feedback," Phys. Fluids A **1**, 1566–1587.

Thomas, F. O., and Prakash, K. M. K. (**1991**). "An experimental investigation of the natural transition of an untuned planar jet," Phys. Fluids A **3**, 90–105.

Thomson, S. L. (**2004**). *Fluid-Structure Interactions Within the Human Larynx*, Ph.D. thesis, Purdue University, West Lafayette, Indiana.

Thomson, S. L., Mongeau, L., and Frankel, S. H. (**2005**). "Aerodynamic transfer of energy to the vocal folds," J. Acoust. Soc. Am. **118**, 1689–1700.

Thomson, S. L., Mongeau, L., Frankel, S. H., Neubauer, J., and Berry, D. A. (**2004**). "Self-oscillating laryngeal models for vocal fold research," in *Proceedings of the Eighth International Conference on Flow-Induced Vibrations* (Ecole Polytechnique, Paris, France), Vol. **2**, pp. 137–142.

Townsend, A. A. (**1976**). *The Structure of Turbulent Shear Flow*, 2nd ed. (Cambridge University Press, Cambridge, UK).

Triep, M., Brücker, C., and Schröder, W. (**2005**). "High-speed PIV measurements of the flow downstream of a dynamic mechanical model of the human vocal folds," Exp. Fluids **39**, 232–245.

Vilain, C., Pelorson, X., and Thomas, D. (**1999**). "Effects of an induced asymmetry on the flow through the glottis in relation to voice pathology," in *Proc. 1st Int. Workshop on Models and Analysis of Vocal Emission for Biomedical Applications (MAVEBA)*, edited by A. Manfredi (University of Florence, Italy).

Westerweel, J. (**1997**). "Fundamentals of digital particle image velocimetry," Meas. Sci. Technol. **8**, 1379–1392.

Winter, M., Lam, J. K., and Long, M. B. (**1987**). "Techniques for high-speed digital imaging of gas concentrations in turbulent flows," Exp. Fluids **5**, 177–183.

Zhang, Z., Mongeau, L., and Frankel, S. H. (**2002**). "Experimental verification of the quasi-steady approximation for aerodynamic sound generation by pulsating jets in tubes," J. Acoust. Soc. Am. **112**, 1652–1663.

Zhang, Z., Neubauer, J., and Berry, D. A. (**2006**). "The influence of subglottal acoustics on laboratory models of phonation," J. Acoust. Soc. Am. **120**, 1558–1569.

Zhao, W., Frankel, S. H., and Mongeau, L. (**2001**). "Large eddy simulations of sound radiation from subsonic turbulent jets," AIAA J. **39**, 1469–1477.